Supporting Information

Scalable Production of Two-Dimensional Metallic Transition Metal Dichalcogenide Nanosheet Powders Using NaCl Templates toward Electrocatalytic Applications

Yahuan Huan,[§,a,b] Jianping Shi,[§,a] Xiaolong Zou,[§,c] Yue Gong,[d,e] Chunyu Xie,[a] Zhongjie Yang,[g] Zhepeng Zhang,[a] Yan Gao,[a] Yuping Shi,[a] Minghua Li,[b] Pengfei Yang,[a] Shaolong Jiang,[a] Min Hong,[a] Lin Gu,[d,e,f] Qing Zhang,[*,a] Xiaoqin Yan,[*,b] and Yanfeng Zhang[*,a]

[a]Department of Materials Science and Engineering, College of Engineering, Peking University, Beijing 100871, China
[b]State Key Laboratory for Advanced Metals and Materials, School of Materials Science and Engineering, University of Science and Technology Beijing, Beijing 100083, China
[c]Tsinghua-Berkeley Shenzhen Institute (TBSI), Tsinghua University, Shenzhen, Guangdong 518055, China
[d]Beijing National Laboratory for Condensed Matter Physics, Institute of Physics, Chinese Academy of Sciences, Beijing 100190, China
[e]School of Physical Sciences, University of Chinese Academy of Sciences, Beijing 100049, China
[f]Songshan Lake Materials Laboratory, Dongguan, Guangdong 523808, China
[g]CAS Key Laboratory of Nanosystem and Hierarchical Fabrication, CAS Center for Excellence in Nanoscience, National Center for Nanoscience and Technology, Beijing 100190, China
[§]Y. Huan, J. Shi, and X. Zou contributed equally.
[*]Correspondence to yanfengzhang@pku.edu.cn, xqyan@mater.ustb.edu.cn, q_zhang@pku.edu.cn

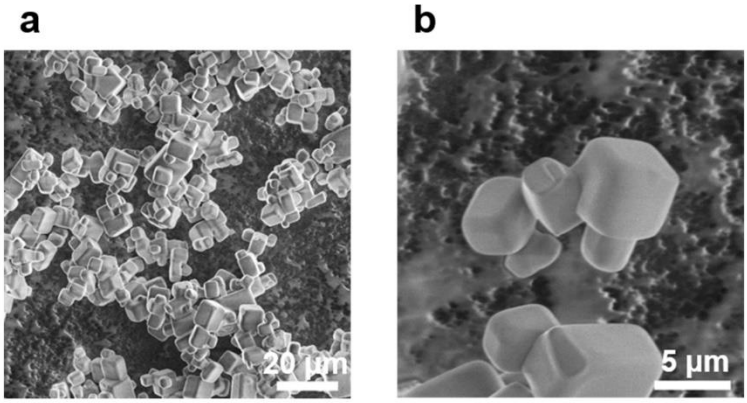

Figure S1. SEM images of the micron-sized cubic NaCl crystals prepared by a recrystallization process. (a) Large-scale SEM image of micron-sized cubic NaCl crystals. (b) Magnified SEM image of micron-sized cubic NaCl crystals.

The micron-sized cubic NaCl crystals were prepared by a recrystallization process. The NaCl salts were dissolved in deionized water to form a saturated solution. After fully dissolved, the NaCl crystals were recrystallized by adding ethanol into the saturated solution. And then, the micron-sized cubic NaCl powder was obtained by follow filtration and drying processes.

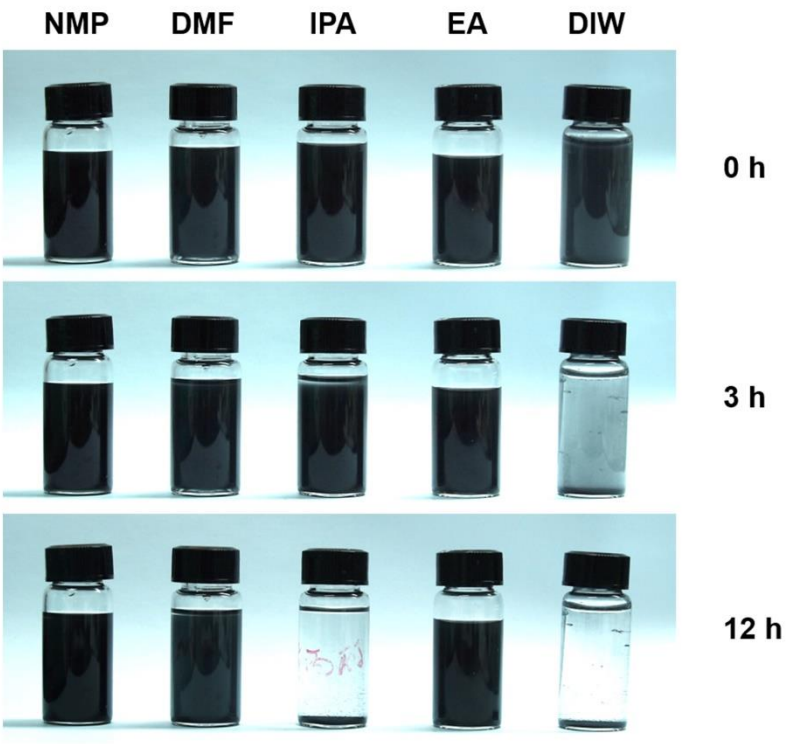

Figure S2. The purified CVD products in various solvents for dispersity measurements.

The purified CVD products were dispersed in various solvents (from left to right: N-Methyl-2-pyrrolidinone (NMP), N, N-Dimethylformamide (DMF), isopropanol (IPA), ethanol (EA), and deionized water (DIW)). Upon dispersed, relatively uniform dispersion can be achieved in various polar solvents.

After 3 h, an obvious precipitation is observed in DIW. After 12 h, the purified CVD products in NMP, DMF, and EA solvents still preserve a relatively uniform dispersion.

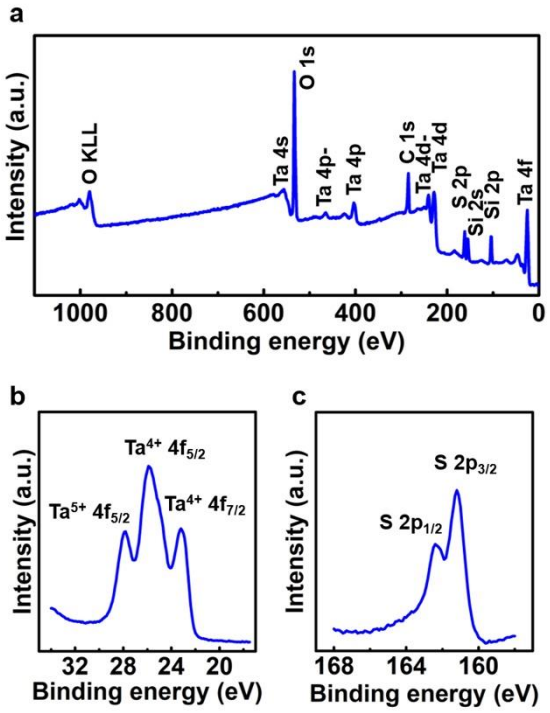

Figure S3. XPS spectra of the purified CVD product of the TaS_2 powder. (a) XPS spectrum of the purified TaS_2 dispersed on SiO_2/Si (acquired over a wide range of binding energies (0-1100 eV)). (b, c) XPS spectra focused on Ta and S elements indicating the formation of TaS_2.

The CVD products were purified by dissolving the NaCl templates in deionized water and performing filtration processes. Then, the sample dispersion was deposited onto SiO_2/Si and dried in vacuum chamber. The XPS measurement was performed to determine the chemical composition of the purified products. The full range XPS data indicated almost no NaCl residues after adequate filtration processes to remove the NaCl templates.

The Ta $4f^{7/2}$ (23.2 eV) and $4f^{5/2}$ (25.7 eV) peaks are assigned to Ta^{4+}, and the S $2p^{3/2}$ (161.2 eV) and $2p^{1/2}$ (162.3 eV) peaks are attributed to S^{2-}. Such results show agreement with that of 1T-TaS_2 reported previously,[1] suggesting the successful synthesis of pure 1T-TaS_2 on the micron-sized cubic NaCl crystals. Another small peak (at 27.8 eV) is in line with that of Ta^{5+}, probably due to the weak surface oxidation of TaS_2.[1] This is because the purification process was finished with the water solution and under atmospheric condition.

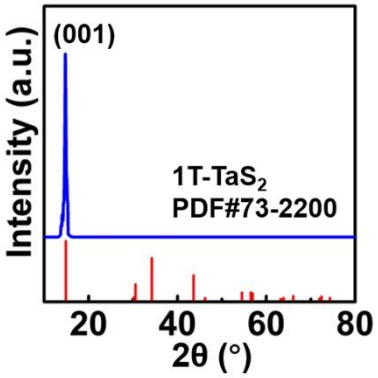

Figure S4. XRD pattern of the purified TaS_2 powder confirming the 1T phase state.

X-ray diffraction (XRD) measurement was conducted to confirm the phase state of the as-grown TaS_2. The diffraction peaks show a good match with the PDF database (#73-2200) of 1T-TaS_2.[2]

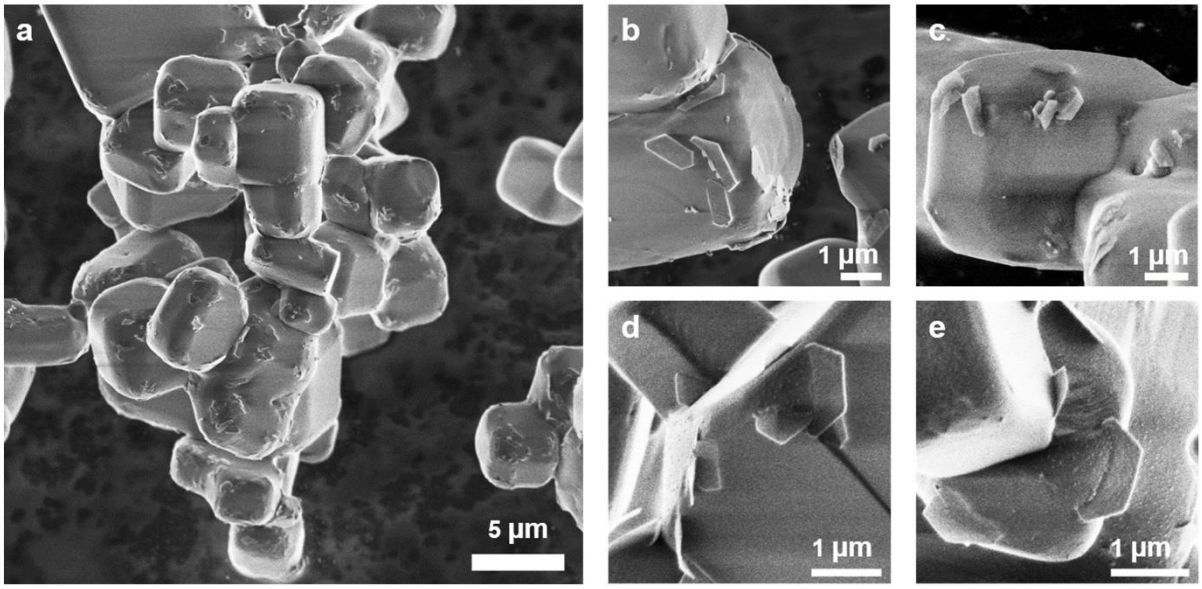

Figure S5. SEM images of as-grown 1T-TaS_2 nanosheets on micron-sized NaCl cubic crystals.

After CVD growth, vertically or horizontally oriented 1T-TaS_2 nanosheets were observed on the edges and corners of the micron-sized cubic NaCl crystals according to the SEM characterizations.

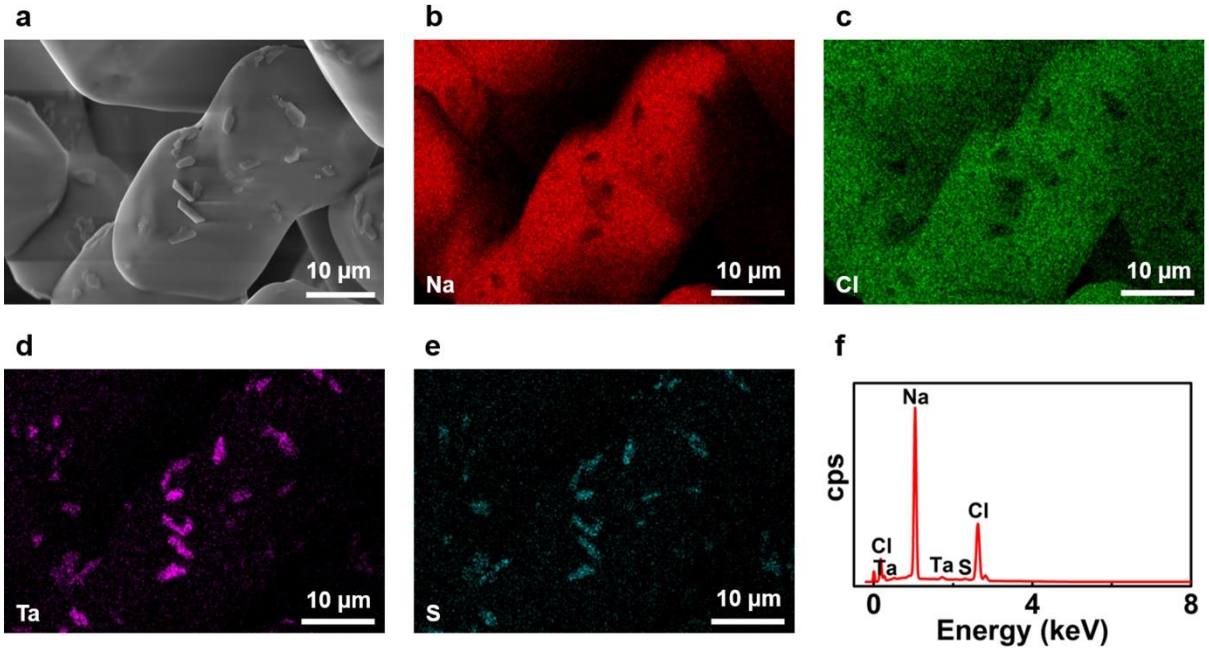

Figure S6. The chemical composition identification of as-grown nanosheets on the micron-sized cubic NaCl crystals. (a) SEM image of as-grown nanosheets on the micron-sized cubic NaCl crystals. (b–d) EDX maps collected from the selected region. (e) Corresponding EDX spectrum showing the elemental composition of the selected region.

The energy dispersive spectroscopy and elemental mapping demonstrate the as-grown nanosheets with Ta and S signals located on the corners of NaCl crystals.

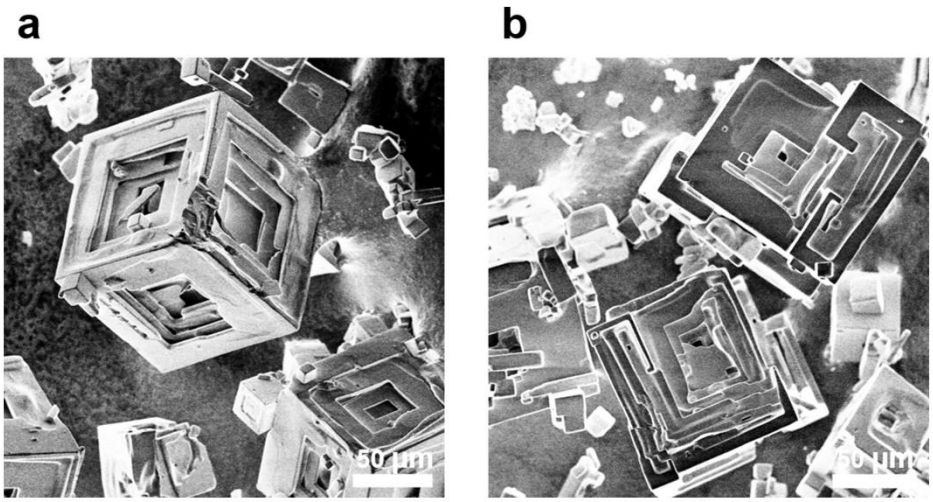

Figure S7. SEM images of the micron-sized multilevel NaCl crystals prepared by a recrystallization process.

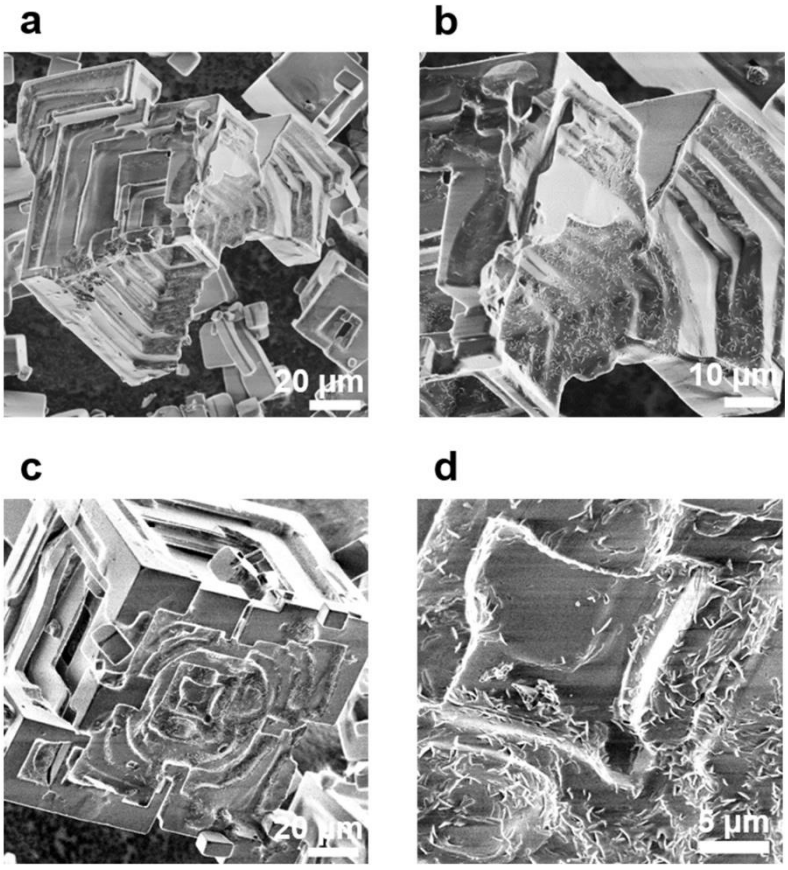

Figure S8. SEM images of as-grown 1T-TaS_2 nanosheets on micron-sized multilevel NaCl crystals.

As shown in the SEM images (Figure S8), the 1T-TaS_2 nanosheets selectively grow vertically on the corners and curved surfaces of micron-sized multilevel NaCl crystals.

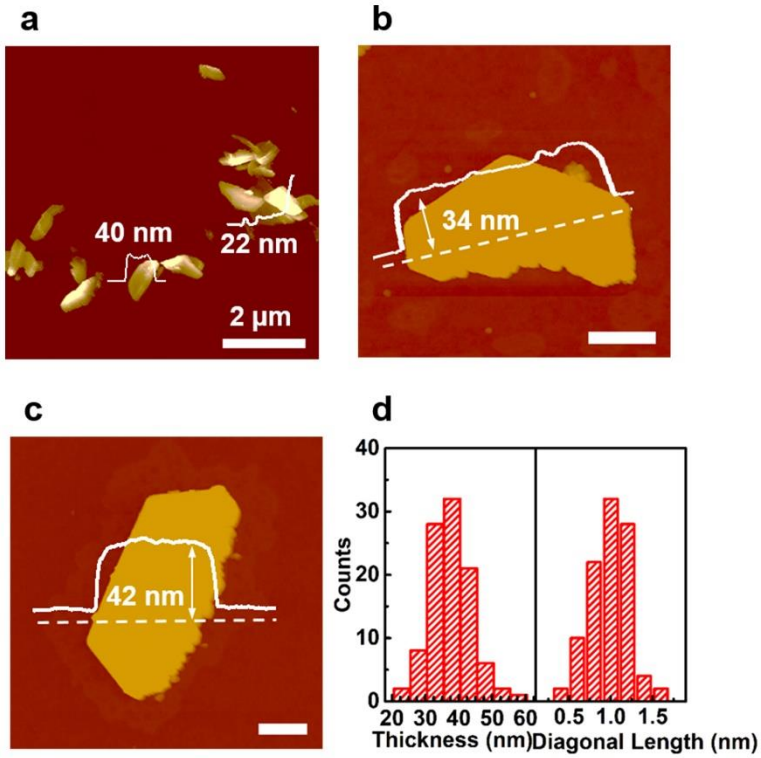

Figure S9. The domain size and thickness distribution of the 1T-TaS_2 nanosheets. (a-c) AFM images and corresponding height profiles of the purified 1T-TaS_2 nanosheets on SiO_2/Si substrates. (d) Statistical calculations of the thickness and diagonal length distributions of the 1T-TaS_2 nanosheets.

Atomic force microscopy (AFM) was employed to evaluate the domain size and thickness of the 1T-TaS_2 nanosheets grown on the micron-sized cubic NaCl crystals. After the purification process, the 1T-TaS_2 nanosheets were dispersed onto SiO_2/Si surface for the AFM test.

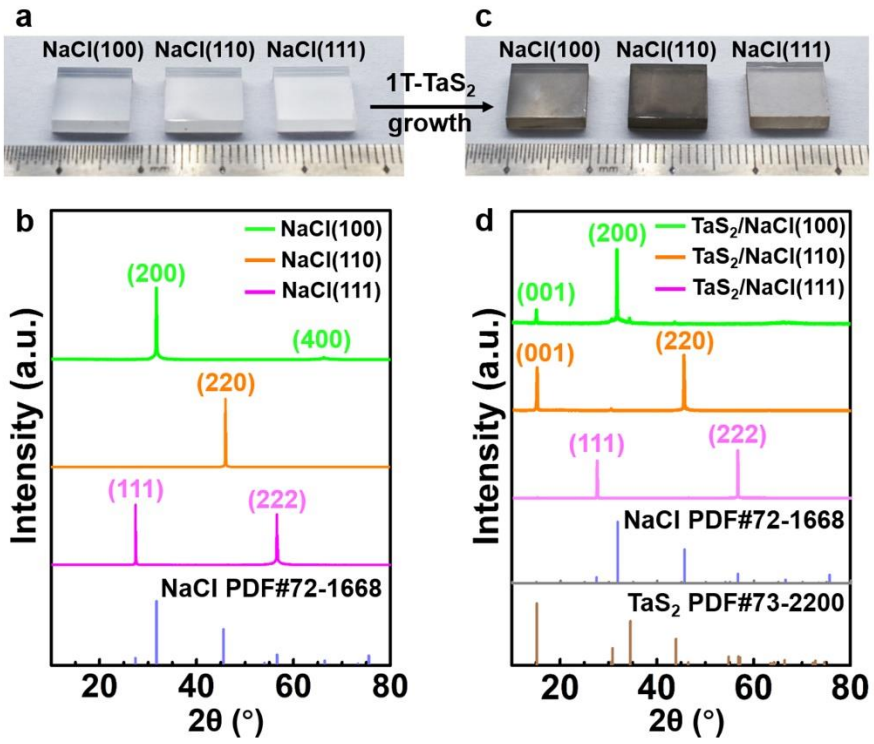

Figure S10. The results of 1T-TaS_2 grown on different NaCl facets of (100), (110) and (111), respectivly. (a) Photograph of NaCl single crystals with different facets. (b) XRD patterns of the NaCl single crystals to confirm their specific facets. (c) Photograph of NaCl single crystals after the growth of 1T-TaS_2. (d) XRD patterns of the NaCl facets after the growth of 1T-TaS_2.

The NaCl single crystals with different facets (size ~1 cm × 1 cm, thickness ~25 mm) were selected as substrates for the growth of 1T-TaS_2, as shown in Figure S10a. XRD measurements were executed to clarify the crystal structures of the NaCl single crystals, and a good match with the PDF database (#72-1668) can be achieved for the different crystals (Figure S10b).

After the CVD processes, the morphology and surface glossiness of the NaCl single crystals remained unchanged (Figure S10c). The XRD patterns of the NaCl single crystals were unaltered after the growth of 1T-TaS_2, clearly demonstrating the steady surfaces of these single crystals throughout the CVD processes (Figure S10d).

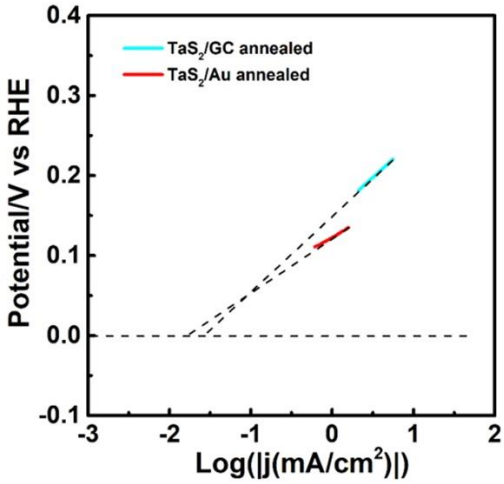

Figure S11. Calculated exchange current densities of annealed 1T-TaS_2 on Au foil and GC electrodes, respectively, by applying an extrapolation method to the Tafel plots.

By applying extrapolation method to the Tafel plots, the exchange current densities (j_0) were calculated as shown in Figure S11. The annealed 1T-TaS_2 samples (on Au foil and GC electrode) exhibit remarkable j_0 values ~19.96 and 20.88 μA cm^{-2}, respectively.

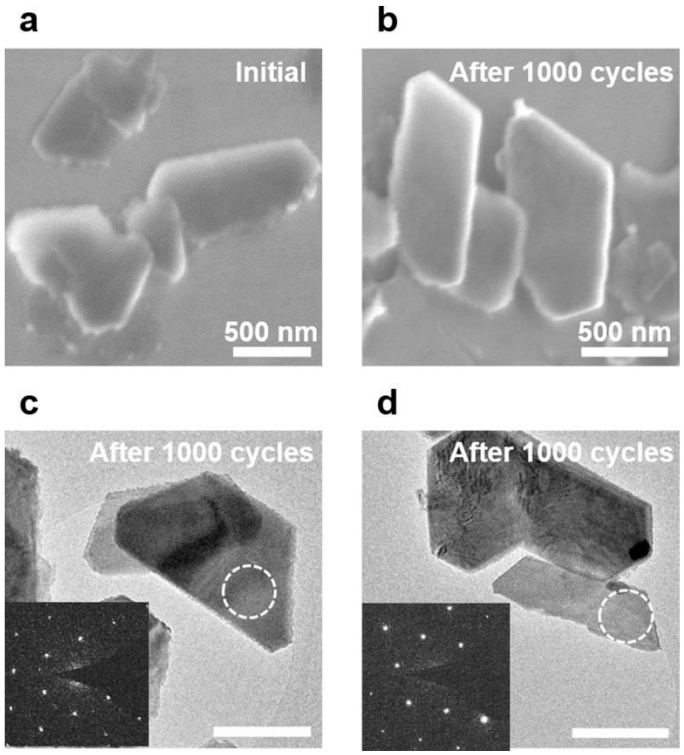

Figure S12. SEM and TEM characterizations of 1T-TaS_2 nanosheets after electrochemical cycles. (a, b) SEM images of 1T-TaS_2 before and after 1000 electrochemical cycles. (c, d) TEM images of 1T-TaS_2 nanosheets after 1000 electrochemical cycles. Insets are the corresponding SAED patterns captured from the circled region in (c, d) with a 200 nm aperture.

The morphologies of 1T-TaS_2 before and after electrochemical cycles are inspected by SEM characterizations (Figure S12a, b). Notably, the 1T-TaS_2 catalysts show invariable morphology after 1000 electrochemical cycles. Moreover, as shown in the typical TEM images and corresponding SAED patterns (Figure S12c, d), the crystal quality of the 1T-TaS_2 also remains unchanged after the electrochemical cycles. All these results indicate the relative high stability of the electrocatalysts throughout the HER measurements.

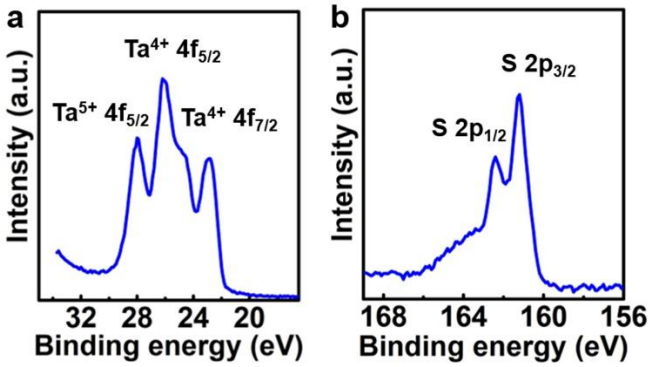

Figure S13. XPS spectra of the 1T-TaS_2 catalyst after 1000 electrochemical cycles. (a, b) XPS spectra focused on Ta and S elements indicating the invariable chemical composition of 1T-TaS_2 throughout the electrocatalytic process.

The XPS characterization of 1T-TaS_2 nanosheets after HER measurements was performed, with the results shown in Figure S13. Notably, there is negligible variation for Ta 4f and S 2p signals, highly suggestive the invariable chemical composition of 1T-TaS_2 nanosheets throughout the electrocatalytic process.

Table S1. Comparison of the HER performances of 1T-TaS_2 and 2H-MoS_2.

Catalyst	Overpotential at 10 mA/cm^2 (mV vs RHE)	Tafel slope (mV/dec)	Exchange current density (μA/cm^2)	Ref.
liquid-phase exfoliated TaS_2 (plasma-treated)	564	135	N/A	21
liquid-phase exfoliated TaS_2	N/A	93.4	N/A	56
Co-doped mesoporous MoS_2 foam	156	74	N/A	54
Strained and vacant 2H-MoS_2	170	60−98	N/A	55
2H-MoS_2 bicontinuous network	285	50	0.69	57
CVD-derived 1T-TaS_2 powders	190−240	61−80	19.96−20.88	this work

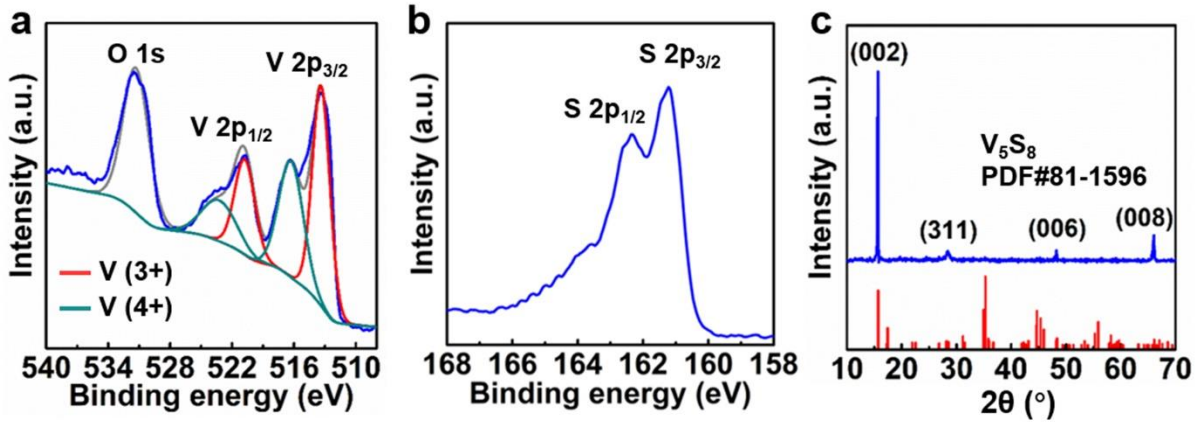

Figure S14. The chemical composition and crystal structure of the purified CVD products. (a, b) XPS spectra focused on V and S elements indicating the formation of V_5S_8. (c) XRD pattern of the purified V_5S_8 powder.

The XPS was used to determine the chemical composition of the purified products. The V $2p^{3/2}$ (513.5 eV) and $2p^{1/2}$ (521.0 eV) peaks are attributed to V^{4+}, and the V $2p^{3/2}$ (516.4 eV) and $2p^{1/2}$ (523.6 eV) peaks are in line with that of V^{3+}. The S $2p^{3/2}$ (161.2 eV) and $2p^{1/2}$ (162.3 eV) peaks can be assigned to S^{2-}.

Such results agree well with that of V_5S_8 reported previously.[3] XRD measurement was also conducted to identify the phase structure of the as-grown samples. The diffraction peaks can be attributed to the (002), (311), (006), and (008) planes of the V_5S_8 crystals, according to the PDF database (#81-1596) of V_5S_8.[3]

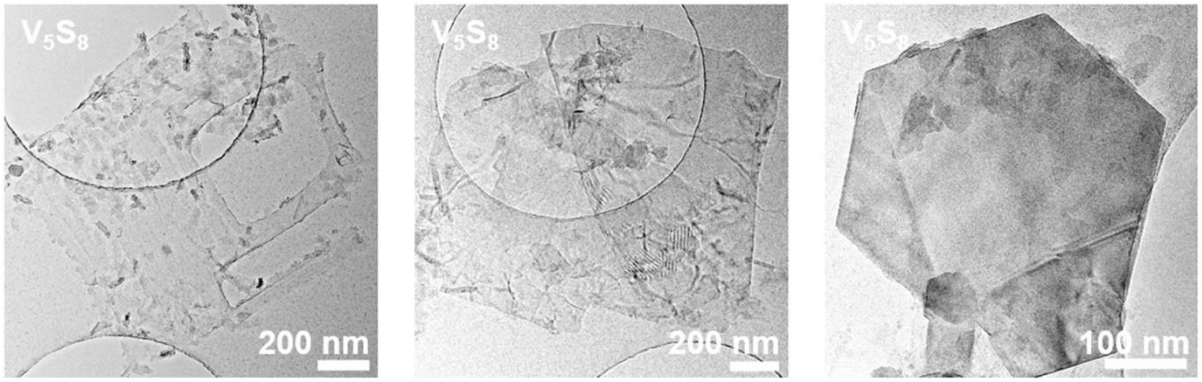

Figure S15. TEM images of the purified V_5S_8 nanosheets dispersed on Cu grids.

To explore the morphology of the CVD-derived V_5S_8 nanosheets, transmission electron microscopy (TEM) was performed on the purified V_5S_8 samples dispersed on Cu grids. Both ultrathin V_5S_8 nanosheets and frame-structured V_5S_8 were observed in TEM images (Figure S15).

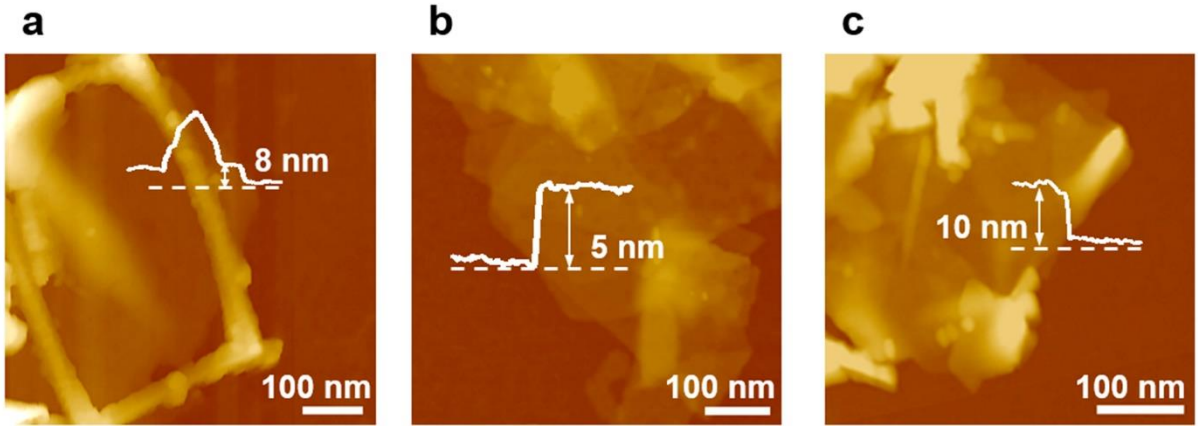

Figure S16. AFM images and the corresponding height profiles of the V_5S_8 nanosheets.

AFM was employed to evaluate the thicknesses of the V_5S_8 nanosheets grown on the micron-sized cubic NaCl crystals. After the purification process, the V_5S_8 nanosheets were dispersed onto SiO_2/Si for the AFM test.

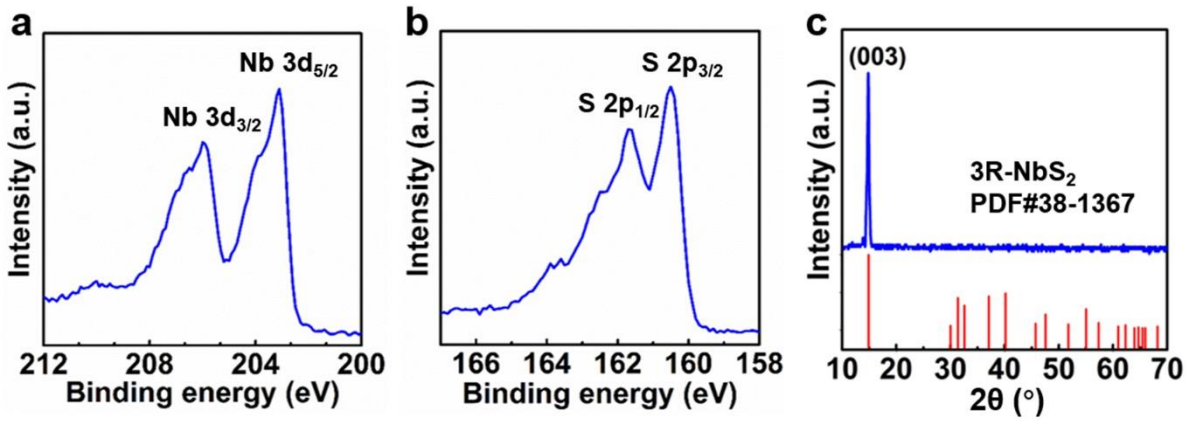

Figure S17. The chemical composition and crystal structure of the purified CVD products. (a, b) XPS spectra focused on Nb and S elements indicating the formation of NbS_2. (c) XRD pattern of the purified NbS_2 powder confirming the 3R phase state.

The chemical composition of the purified products was determined by XPS characterizations. The Nb $3d^{5/2}$ (203.1 eV) and $3d^{3/2}$ (206 eV) peaks are assigned to Nb^{4+}, and the S $2p^{3/2}$ (160.5 eV) and $2p^{1/2}$ (161.6 eV) peaks are attributed to S^{2-}. Such results show agreement with that of NbS_2 reported previously,[4] thus indicating the successful synthesis of NbS_2 on the micron-sized cubic NaCl crystals. The XRD measurement was executed to confirm the phase state of the as-grown NbS_2. The typical peaks show a good match with the PDF database (#38-1367) of 3R-NbS_2.[5]

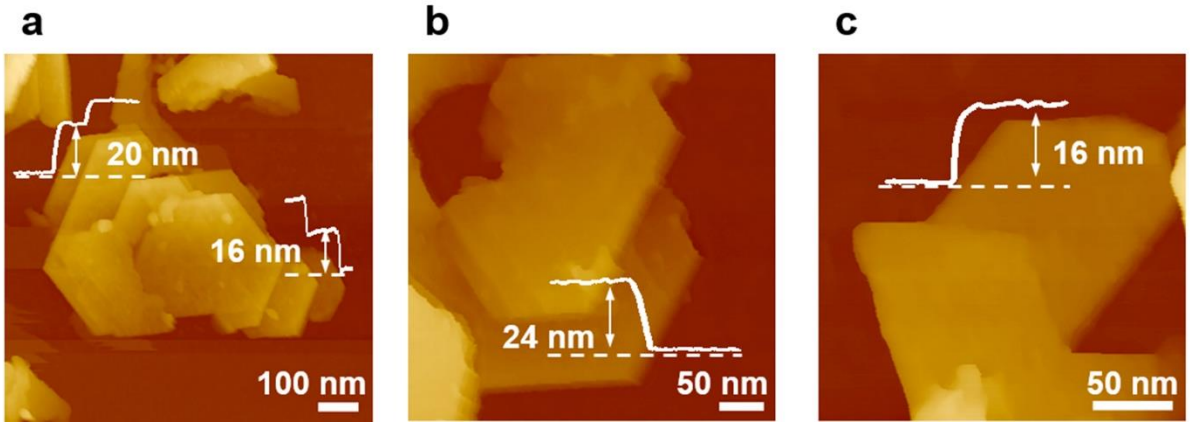

Figure S18. AFM images and the corresponding height profiles of the NbS_2 nanosheets.

REFERENCES

(1) Y. Huan, J. Shi, X. Zou, Y. Gong, Z. Zhang, M. Li, L. Zhao, R. Xu, S. Jiang, X. Zhou, M. Hong, C. Xie, H. Li, X. Lang, Q. Zhang, L. Gu, X. Yan, Y. Zhang, *Adv. Mater.* **2018**, *30*, 1705916.

(2) J. Pan, C. Guo, C. Song, X. Lai, H. Li, W. Zhao, H. Zhang, G. Mu, K. Bu, T. Lin, X. Xie, M. Chen, F. Huang, *J. Am. Chem. Soc.* **2017**, *139*, 4623.

(3) Q. Ji, C. Li, J. Wang, J. Niu, Y. Gong, Z. Zhang, Q. Fang, Y. Zhang, J. Shi, L. Liao, X. Wu, L. Gu, Z. Liu, Y. Zhang, *Nano Lett.* **2017**, *17*, 4908.

(4) H. Bark, Y. Choi, J. Jung, J. H. Kim, H. Kwon, J. Lee, Z. Lee, J. H. Cho, C. Lee, *Nanoscale* **2018**, *10*, 1056.

(5) W. Ge, K. Kawahara, M. Tsuji, H. Ago, *Nanoscale* **2013**, *5*, 5773.